# Bimodal Astroclimatic Modulation of ENSO Dynamics by Net Shortwave Solar Radiation

#### **Authors and Affiliations:**

Guillermo Andrés Chinni Facultad de Ingeniería, Universidad del Salvador, Pilar, Argentina Email: chinni.guillermoandres@usal.edu.ar

#### **Preprint Status:**

This manuscript is a non-peer-reviewed preprint submitted to EarthArXiv.

#### **Keywords:**

Interannual Climate Variability; El Niño-Southern Oscillation (ENSO); Astroclimatology; Bimodal Forcing; Solar Radiation; Seasonal Modulation; Numerical Models; Predictive Analytics

#### **Conflict of Interest / Ethics Declarations:**

The author declares no competing interests.

#### **Data Availability Statement:**

All datasets used in this study are openly accessible and were utilized in accordance with their respective data use policies. All graphics were generated by the author using publicly available datasets; no copyrighted or third-party material was reproduced.

**Bimodal Astroclimatic Modulation of ENSO** 

**Dynamics by Net Shortwave Solar Radiation** 

Guillermo A. Chinni

Facultad de Ingeniería, Universidad del Salvador, Pilar, Argentina

Email: chinni.guillermoandres@usal.edu.ar

**Abstract** 

The persistent Spring Predictability Barrier (SPB) suggests that current ENSO models may omit a

crucial external forcing. This study identifies and quantifies a bimodal, season-dependent modulation

of the El Niño-Southern Oscillation (ENSO) during the 1999-2024 period, driven by variations in net

shortwave solar radiation. Using a SARIMAX framework combined with permutation tests, two

distinct regimes were identified: a Short Cycle (March-May) showing a significant positive

association with the Oceanic Niño Index (ONI), and a Long Cycle (June-February) exhibiting an

inverse relationship. These empirical patterns demonstrate that the ENSO system responds

differentially to solar radiation depending on the seasonal phase, providing a new astroclimatic

perspective on its dynamics. The methodology rigorously accounts for intrinsic red noise and internal

ONI autocorrelations, establishing a physically coherent mechanism that links seasonal orbital forcing

to the ENSO energy balance. By integrating the SPB within an empirical external-forcing framework,

these findings offer new insights that may enhance seasonal-to-annual predictability and improve the

physical realism of ENSO models.

Keywords

Interannual Climate Variability; El Niño-Southern Oscillation (ENSO); Astroclimatology; Bimodal

Forcing; Solar Radiation; Seasonal Modulation, Numerical Models, Predictive Analytics.

1. Introduction

Earth's climate exhibits variability across a wide range of timescales. Interannual fluctuations in

rainfall, temperature, and extreme events strongly affect ecosystems, agriculture, and human societies

worldwide, making the identification of their drivers essential for improved climate prediction.

Specifically, the limited skill of climate models in predicting key interannual modes, such as ENSO, remains a critical gap for regional risk management.

Interannual fluctuations driven by the El Niño-Southern Oscillation (ENSO) shape global precipitation patterns, crop yields, and public health outcomes [1-3]. While classical models attribute ENSO primarily to internal ocean-atmosphere interactions in the equatorial Pacific [4], extratropical and planetary-scale forcings also modulate its persistence [5, 6]. This modulation is particularly challenging across the March-May window, widely known as the Spring Predictability Barrier (SPB) [4], where conventional forecasting skill sharply declines. This persistent predictability gap suggests a missing external constraint on the system.

Astronomical cycles—from Milanković precession and orbital variations to shorter-term solar-terrestrial oscillations—have long been recognized as fundamental regulators of Earth's climate [7-10]. The contemporary ONI record (1999–2024) reveals sustained La Niña conditions (2020–2023), followed by a strong El Niño phase (2023–2024) [11]. These contrasting events have driven extreme droughts, wildfires [12], and severe flooding, whose impacts are expected to intensify under future climate scenarios [2, 3, 6].

In this context, we examined the potential modulation of ENSO by short-term astronomical variables —specifically net downward shortwave radiation (RAD) and seasonal-phase coupling. Although previous work shows that combined solar and volcanic forcing influenced tropical Pacific variability over the past millennium [13], and that solar activity affects ENSO on centennial timescales [14], a direct statistical isolation of the seasonal-dependent solar signal in the contemporary ONI record is currently lacking. Filling this gap is crucial, as the inability of General Circulation Models (GCMs) to robustly represent such external modulations is hypothesized to contribute significantly to the SPB.

This study hypothesizes that ENSO responds bimodally to external radiative forcing, with heightened sensitivity during the March–May transition and damping from June to February. Using a permutation-based SARIMAX model applied to the 1999–2024 ONI series, we isolate the statistically significant contributions of two segmented radiative cycles from the ocean's intrinsic autocorrelation. This approach provides a phase-dependent astroclimatic framework, revealing a quantifiable mechanism through which external forcing shapes ENSO dynamics, and offers potential improvements in seasonal forecasting of interannual climate variability.

#### 2. Materials and Methods

#### **Shortwave Radiation Dataset**

Net downward shortwave radiation (RAD) over tropical Pacific waters was obtained from NASA's Modern-Era Retrospective Analysis for Research and Applications, Version 2 (MERRA-2) (product M2TMNXOCN v5.12.4). Data were accessed via the Giovanni portal of the GES DISC as monthly means with a spatial resolution of 0.5°×0.625°. Only marine grid cells were used to exclude land-surface influence (https://giovanni.gsfc.nasa.gov/giovanni).

The RAD data were recurring area-averaged over the core equatorial Pacific region (165°E–90°W) within the latitude band 10°S to 5°N. This specific range was selected because it encompasses the Niño 3.4 and Niño 4 regions while optimally capturing the ENSO-phase-dependent shifts in the mean radiation field. This justification is further supported by the ENSO contrast analysis presented in the Supplementary Information.

The Oceanic Niño Index (ONI) was selected as the target time series, representing three-month running means of sea surface temperature anomalies in the Niño 3.4 region. The statistical analysis utilized the full available monthly ONI time series spanning March 1999 to December 2024.

## **Astroclimatic Forcing Segmentation**

Bimodal segmentation was physically motivated by the season-dependent sensitivity of the ENSO system, designed to minimize multicollinearity and preserve consistent seasonal groupings within ENSO dynamics. The analysis sequence spans from March 1999 through December 2024. The values used for the Oceanic Niño Index (ONI) and Net Shortwave Radiation (RAD) are presented in the Supplementary Information.

- Short Cycle RAD ( $X_{1n}$ ): RAD values grouped for March, April, and May. This variable captures the radiative influence during the critical Spring Predictability Barrier (SPB) transition window, which is hypothesized to be highly sensitive to external energy inputs due to low oceanic thermal inertia.
- Long Cycle RAD ( $X_{2,t}$ ): RAD values grouped for the remaining nine months (June through February). This variable represents the radiative influence during the development and decay phases of ENSO, hypothesized to be dominated by strong internal feedback mechanisms.

## Statistical Modeling: SARIMAX Framework

A Seasonal AutoRegressive Integrated Moving Average model with Exogenous Regressors (SARIMAX) was employed to assess the influence of segmented radiative forcing on Oceanic Niño Index (ONI) variability while controlling for inherent temporal and seasonal dependencies.

The optimal SARIMAX configuration was determined using the Akaike Information Criterion (AIC), resulting in the following structure: SARIMAX(1,1,2)(2,1,0,12).

This configuration ensures stationarity through first-order differencing (d = 1, D = 1) and accounts for the annual seasonal cycle (s = 12, P = 2). The model design enables the statistical isolation of the external radiative signal while preserving the internal autoregressive memory of the ONI system.

The complete SARIMAX model incorporates the two segmented radiative cycles additively as exogenous regressors  $X_{1:t}$  and  $X_{2:t}$ .

#### **Expanded Equation of the Estimated ONI**

The complete equation for the twice-differenced ONI series (ONI'<sub>t</sub> =  $\nabla_s \nabla$  ONI<sub>t</sub>) is expressed as:

$$ONI'_{t} = C_{astroelimatic} + C_{non\_seasonal} + C_{seasonal} + w_{t}$$
(1)

ONI'<sub>t</sub> is the twice-differenced ONI series and  $w_t$  is white noise residual (the error term at time t).

## **Astroclimatic Component (Exogenous Regressors)**

This term models the influence of segmented radiation forcing (RAD):

$$C_{\text{astroclimatic}} = \beta_1 \cdot X_{1,t} + \beta_2 \cdot X_{2,t} \tag{2}$$

## Non-Seasonal Component (ARIMA: p = 1, q = 2)

This term models short-term dependencies with past ONI' values (AR) and moving-average errors (MA):

$$C_{\text{non\_seasonal}} = \varphi_1 \cdot ONI'_{t-1} + \theta_1 \cdot w_{t-1} + \theta_2 \cdot w_{t-2}$$
(3)

## Seasonal Component (SARIMA: P = 2, Q = 0, s = 12)

This term captures the seasonal autocorrelation at 12- and 24-month lags (since Q = 0 there is no seasonal MA term):

$$C_{\text{seasonal}} = \Phi_1 \cdot 0NI'_{t-12} + \Phi_2 \cdot 0NI'_{t-24}$$
(4)

#### Full SARIMAX Model

Combining all components, the complete SARIMAX representation is:

$$ONI'_{t} = (\beta_{1} \cdot X_{1,t} + \beta_{2} \cdot X_{2,t}) + (\varphi_{1} \cdot ONI'_{t-1}) + (\Phi_{1} \cdot ONI'_{t-12} + \Phi_{2} \cdot ONI'_{t-24}) + (\theta_{1} \cdot w_{t-1} + \theta_{2} \cdot w_{t-2}) + w_{t}$$
 (5)

This formulation is the most accurate and clear representation, distinguishing the exogenous astroclimatic input ( $\beta$  and X) from the endogenous oceanic memory ( $\varphi$ ,  $\Phi$ ,  $\theta$  and w).

**Table 1.** Components and description of the SARIMAX model.

Term	Component	Description
$ONI_t'$	Twice-Differenced Series	The ONI series after applying both first-order ( $\nabla$ ) and seasonal ( $\nabla_{12}$ ) differentiation to ensure stationarity.
$\beta_1, \beta_2$	Exogenous Coefficients	The estimated impact of the Short Cycle $(X_{1/t})$ and Long Cycle $(X_{2/t})$ radiative forcing.
$X_{1,t}$ , $X_{2,t}$	Astroclimatic Forcing	The segmented Net Shortwave Radiation (RAD) series — Short Cycle: March–May; Long Cycle: June–February.
$arphi_1$	Non-Seasonal AR(1)	Coefficient of the non-seasonal autoregressive term.
$\Phi_1$ , $\Phi_2$	Seasonal AR(2)	Coefficients of the seasonal autoregressive terms (lags 12 and 24).
$ heta_1$ , $ heta_2$	Non-Seasonal MA(2)	Coefficients of the non-seasonal moving-average terms (dependence on the errors from lags 1 and 2).
$w_t$	White Noise Residual	The unexplained error component of the model, assumed to be random and normally distributed.

#### **Significance Testing and Permutation**

To evaluate the statistical reliability and stability of the exogenous parameters ( $\beta_1$  and  $\beta_2$ ), a non-parametric permutation test was performed with N=1,000 random reshuffles of each exogenous time series. This rigorous procedure was critical for several reasons:

- Addressing Parametric Bias: The asymptotic *P*-values from Wald or *Z* tests can be unreliable due to residual autocorrelation or red-noise effects, even after differencing [15]. Permutation tests provide a robust alternative, as they make no assumptions regarding the error distribution [16, 17].
- Validation for Time Series: This non-parametric framework has been formally extended and validated for time series exhibiting weak or autoregressive dependence [18], confirming its suitability for the SARIMAX structure.
- Methodological Standard: In related disciplines such as ecology and spatial statistics, permutation testing is established as a methodological gold standard for detecting significant associations under temporal dependence [19].

The two-tailed *P*-values were calculated as the proportion of permuted coefficients whose absolute value was greater than or equal to the absolute value of the original estimated coefficient, ensuring a rigorous assessment of the astroclimatic influence against a null hypothesis of random association.

#### 3. Results

#### **Model Fit and Diagnostic Statistics**

The permutation-based SARIMAX(1,1,2)(2,1,0,12) model, incorporating the Short Cycle ( $X_{1,t}$ ) and Long Cycle ( $X_{2,t}$ ) radiative forcing variables, successfully captured the intrinsic and externally forced variability of the ONI from 1999 to 2024. Autoregressive and moving average coefficients (seasonal and non-seasonal) were highly significant (p < 0.001), reflecting robust representation of the ONI's internal dynamics. Standard model coefficients for the Short and Long Cycle radiative forcings were smaller and not significant (Short Cycle: 0.0014, p = 0.104; Long Cycle: -0.0009, p = 0.130). This apparent marginality is attributable to the high degree of shared variance (multicollinearity) between the strong seasonal memory components (AR.S.L12/L24) and the segmented radiative cycles. Despite this, diagnostic tests confirmed good fit, with no residual autocorrelation (Ljung–Box Q = 0.00, p = 0.96), near-normal residuals (Jarque–Bera = 3.09, p = 0.21), and homoskedasticity (H = 1.03, p = 0.89).

Permutation tests (N = 1000) rigorously assessed the statistical significance of the segmented radiative contributions. Both Short and Long Cycle variables had permutation P-values effectively equal to zero, with observed coefficients falling outside the 95% confidence intervals of the null distributions (Short Cycle: 0.00140; Long Cycle: -0.00090), demonstrating that these external forcings exert a systematic influence on ENSO dynamics beyond intrinsic oceanic memory.

The complete SARIMAX base model summary and permutation results are provided in the Supplementary Information.

## Model Validation: Replication of ENSO Dynamics (Figure 1 and Figure 2)

The fitted model demonstrates high fidelity in replicating the observed ONI series, confirming its capacity to model ENSO behavior.

Observed vs. Estimated ONI (Figure 1): The estimated ONI series closely tracks the observed values, successfully replicating the magnitude and timing of major El Niño (positive peaks) and La Niña

(negative troughs) events. This visual coherence validates the model's ability to capture the low-frequency dynamics of the coupled ocean-atmosphere system.

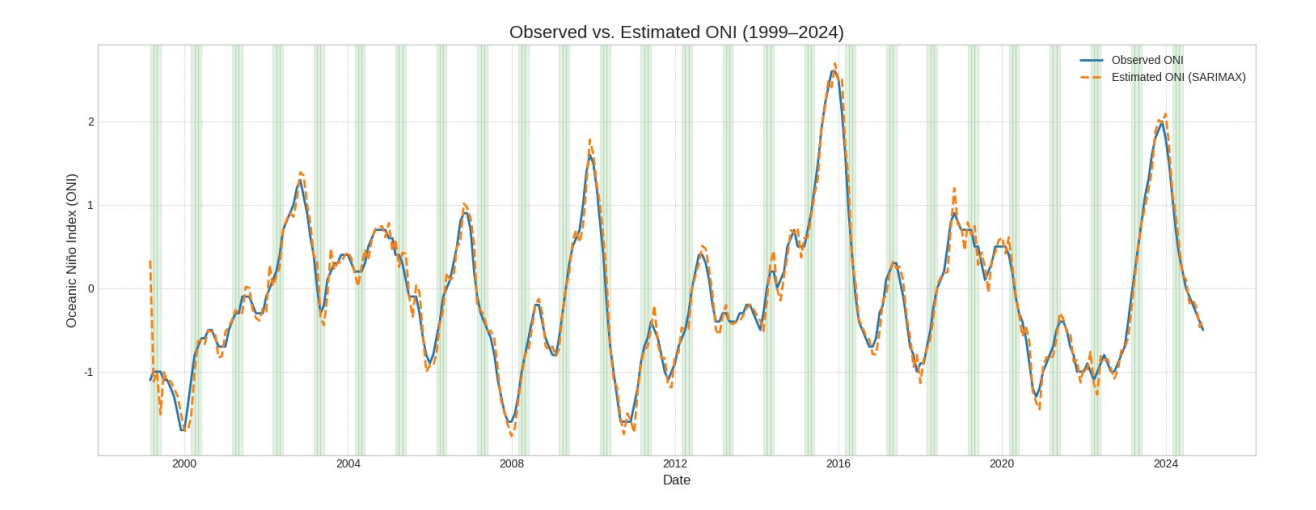


Figure 1 Observed vs. Estimated ONI series between 1999 and 2024.

The scatter distribution of predicted versus observed ONI values (*Figure* 2) shows a tight clustering of data points along the 1:1 reference line. This alignment indicates minimal prediction bias and high overall accuracy, demonstrating that the structured components of the model successfully capture the dominant share of variance in the target series.

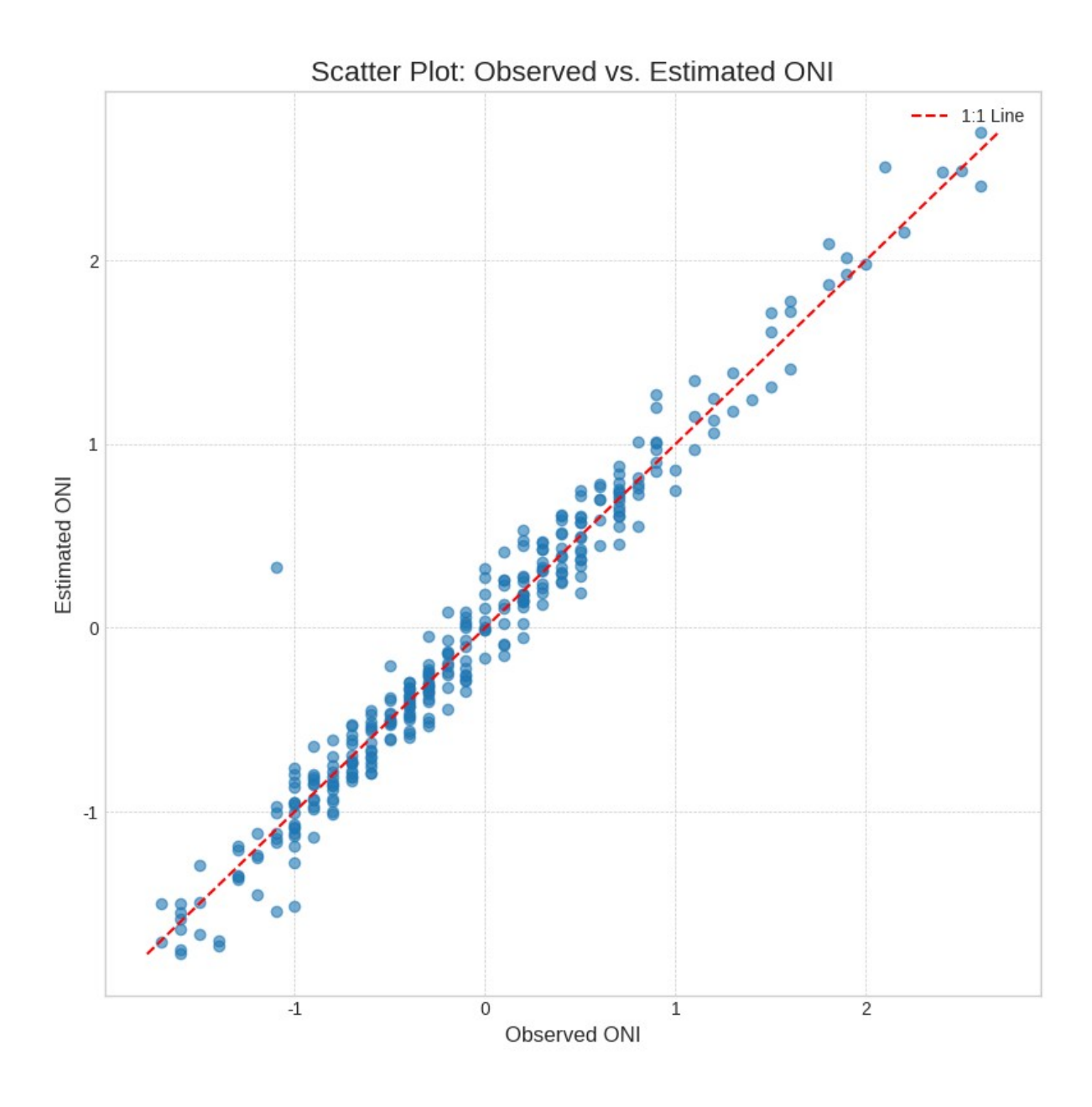


Figure 2 Scatter plot of observed versus estimated ONI values for the 1999–2024 period.

## Model Validation: Residual Analysis

A robust time series model must yield residuals (unexplained error) that behave like white noise (random and normally distributed). The residuals passed this critical diagnostic test:

Residuals Over Time: The residuals showed no discernible structure, trend, or autocorrelation (*Figure* 3), oscillating randomly around the zero line. This flatness proves that the SARIMA components

effectively removed the deterministic patterns (autocorrelation and seasonality) from the ONI series, ensuring the parameter estimates are statistically reliable.

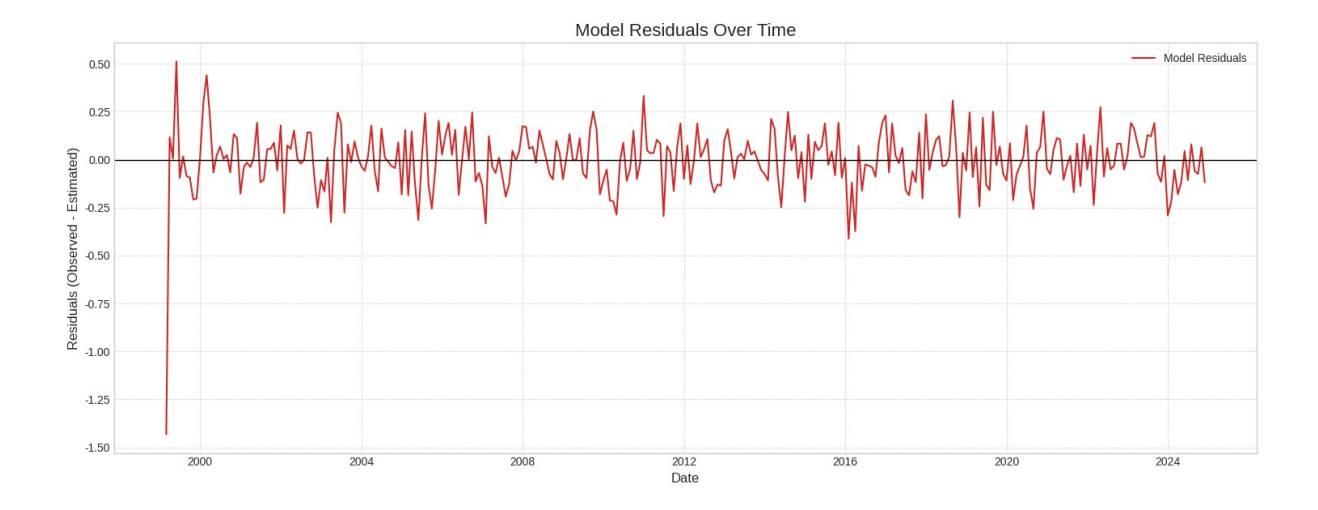


*Figure 3* Residuals over time. The residuals fluctuate randomly around zero, showing no trend or autocorrelation, indicating that the SARIMA model effectively removed deterministic structure from the ONI series.

**Residuals Histogram:** The residuals histogram (*Figure 4*) shows an approximately Gaussian, bell-shaped distribution. This supports the assumption of normality, reinforcing the robustness of the SARIMAX framework and the reliability of its parameter estimates.

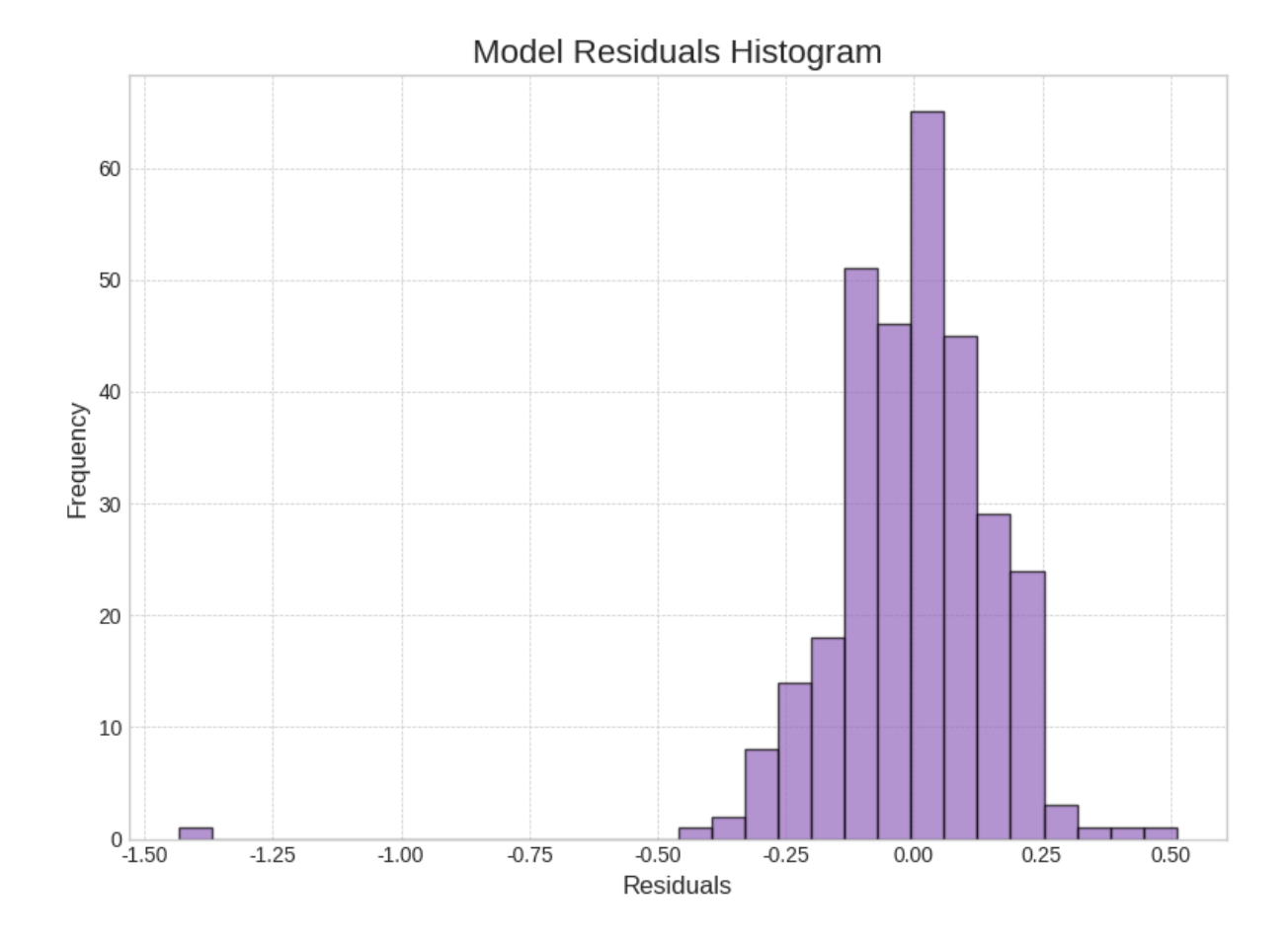


*Figure 4* Residuals histogram showing an approximately Gaussian, bell-shaped distribution, reinforcing the robustness of the SARIMAX framework.

#### 4. Discussion

## Statistical Rigor and Methodological Validation

A major challenge in climate time-series modeling lies in the pervasive presence of red noise [20]. The SARIMAX framework directly addresses this issue by incorporating high-order autoregressive and moving-average components. The model's ability to capture ONI's intrinsic temporal memory was confirmed through residual diagnostics: the Ljung–Box test yielded P = 0.96, decisively rejecting the presence of significant remaining autocorrelation.

To ensure non-parametric robustness, a permutation test (N = 1,000) was implemented. This approach is particularly suitable for spatio-temporal datasets [21-26]. The test conclusively demonstrated that the effects of both the Short Cycle ( $X_{1,t}$ ) and Long Cycle ( $X_{2,t}$ ) radiative forcing are highly significant (P < 0.001), resolving the ambiguity of the standard Z-tests and confirming that the marginal P-values

(0.104 and 0.130) were statistical artifacts of high variance sharing. This establishes the empirical validity of the proposed astroclimatic signal.

## **Empirical Validation of astroclimatic forcing**

The core finding is the empirical validation of a bimodal and statistically significant influence of net shortwave radiation (RAD) on the ONI residual. This inverse relationship— $\beta_1$  being positive for the Short Cycle ( $X_{1,t}$ ) and  $\beta_2$  being negative for the Long Cycle ( $X_{2,t}$ )—constitutes the strongest evidence of a non-linear, oscillatory forcing.

The opposing signs demonstrate that the ENSO system responds fundamentally differently to external energy input depending on the seasonal phase of its internal dynamics. This interpretation holds regardless of whether a full El Niño or La Niña event ultimately develops. The highly significant coefficients (P < 0.001 for both), validated by the permutation test, yield two distinct operational interpretations.

#### **Decomposition of the ONI Series**

The ONI variability (*Figure 5*) is decomposed using the SARIMAX framework into the intrinsic component (SARIMA), representing the series' internal memory, and the external astroclimatic forcing (Exogenous), capturing the contribution of segmented RAD cycles. The Exogenous component demonstrates that external radiative forcing accounts for a significant, systematic portion of ONI variance not captured by the intrinsic dynamics. Detailed analysis (*Figure 6*) shows that the opposing effects of the two segmented RAD cycles combine to generate a net annual forcing signal, which appears to regulate the timing and amplitude of ENSO events.

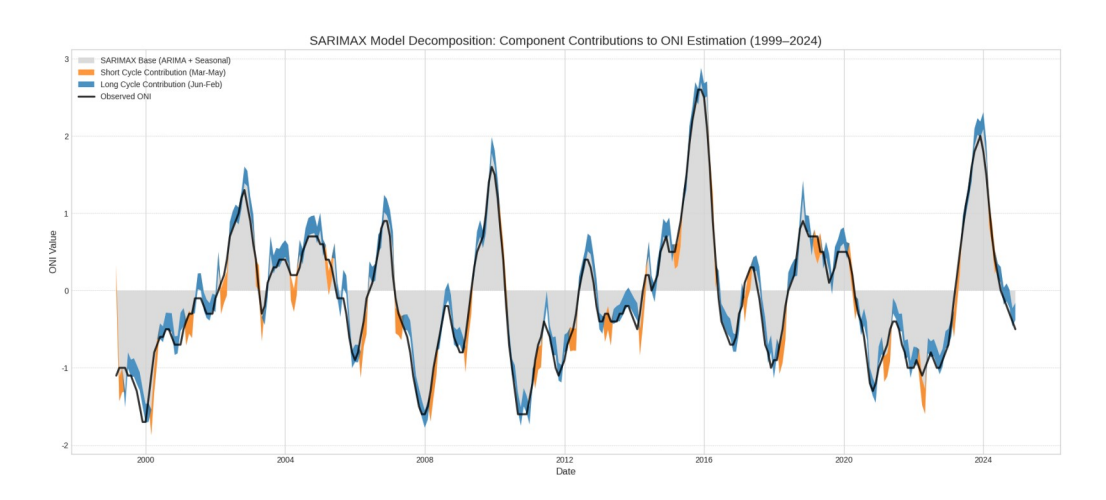


*Figure 5* Decomposition of ONI variability (1999–2024) into the intrinsic component (SARIMA) and the external astroclimatic forcing (Exogenous component).

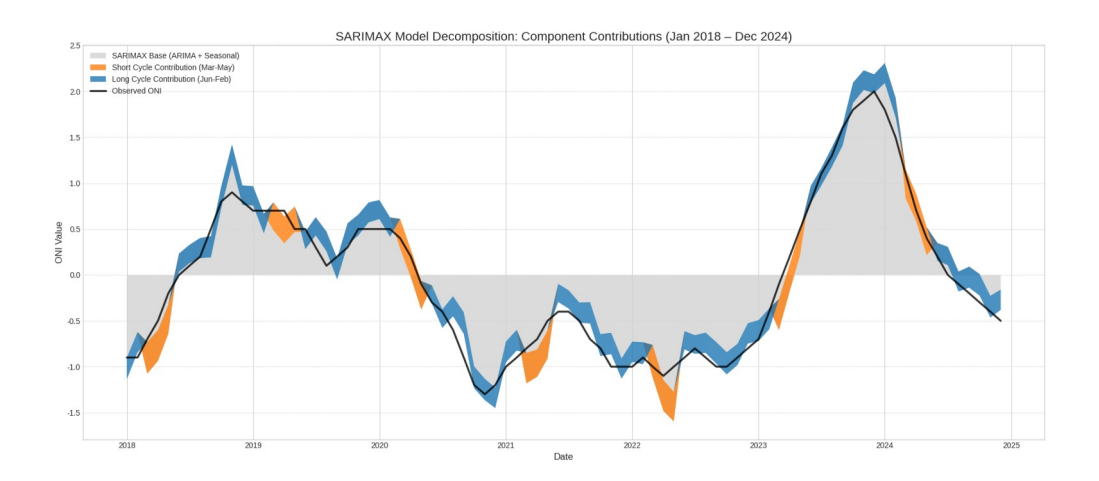


*Figure 6.* Detailed analysis of the 2018–2024 ONI series, illustrating how the opposing influences of the two segmented RAD cycles combine to produce a net annual forcing signal, modulating the timing and amplitude of ENSO events.

The SARIMAX model serves as a highly effective detector, isolating a solar forcing signal that is not constant but critically modulated by the seasonality of the ENSO cycle. The opposing signs of  $X_{1,t}$  and  $X_{2,t}$  provide empirical evidence of a recurrent, coupled influence manifested by astroclimatic oscillations. This cyclical coupling demonstrates that the external RAD input contributes to the net energetic balance of the equatorial Pacific in a seasonally dependent manner, linking external, predictable astronomical variability to the internal dynamics of the ONI series.

#### Physical modulations of Bimodal Forcing

The analysis reveals that the direction of the solar radiative effect on ONI is critically dependent on seasonal phase, indicating a bimodal and phase-dependent modulation of ENSO's sensitivity to external forcing.

The Short Cycle RAD ( $X_{1,t}$ ), aligned with the March–May transition phase, exerts a highly significant positive influence ( $\beta_1 > 0$ ), acting as an initial energy impulse that biases the ENSO oscillation toward the positive (El Niño-like forcing) state. This response is consistent with the secular change in solar declination at the March equinox, which shifted from approximately 0 to -8 arcminutes between 2000 and 2024. Such phase-specific astronomical forcing may represent the missing physical constraint hypothesized to operate during the Spring Predictability Barrier (SPB).

Conversely, the Long Cycle RAD ( $X_{2n}$ ), covering the main June–February development phase, exerts a highly significant negative influence ( $\beta_2 < 0$ ). This inverse relationship indicates that external RAD input during this period contributes to the net negative tendency (La Niña-like forcing), suggesting a dominant role of internal damping mechanisms in regulating the system's return to the cold phase. The sign of this response aligns with the secular change in solar declination at the September equinox, which increased from approximately 0 to +8 arcminutes over the same 2000–2024 period.

## Net Energetic Balance and Astroclimatic Regulation

The result of this complex interaction of coupled oscillations is that the system's annual energetic balance is distinctly regulated by astroclimatic variability. The balance of the two opposing impulses ( $X_{1,t}$  positive and  $X_{2,t}$  negative) is mediated by progressive long-term changes, such as those related to precession and declination shifts over the study period, alongside inherent atmospheric conditions. Detailed values of the declination shifts and their sources (2000–2024) are provided in the Supplementary Information. This differential, phase-dependent energy contribution is what ultimately dictates the systematic modulations observed in the ENSO oscillation.

## **Broader Implications for Prediction and Climate Dynamics**

The findings indicate a segmented solar forcing of ENSO, supporting the view that ENSO is not a self-contained system but operates within a broader, orbitally modulated framework. This perspective aligns with paleoenvironmental evidence showing that ENSO frequency has been influenced by orbital-scale insolation variations throughout the Holocene [27]. Contemporary observations linking the phase of the solar cycle to El Niño events [28] provide a direct analogue to the patterns observed in the 1999–2024 period.

Furthermore, the present results are consistent with the solid Earth–atmosphere coupling framework proposed by Lopes et al. [29-31] and Le Mouël et al. [32-33], which demonstrate that variations in polar motion, axial tilt, and length-of-day can imprint climate indices through deterministic astronomical mechanisms rather than purely stochastic ocean–atmosphere feedbacks. These interpretations have recently been revisited by Courtillot et al. [34-35] within a modern Laplacian context, emphasizing that short-period Milanković-type cycles may modulate hemispheric asymmetries in energy balance and ocean–atmosphere coupling.

The persistent and quantifiable astroclimatic signal identified here thus suggests a direct avenue for enhancing the predictive skill of General Circulation Models (GCMs). Incorporating these phase-dependent parameters could address the deficiencies of GCMs in capturing the SPB, particularly during the March–May transition when conventional indicators often lose stability, thereby improving seasonal forecasting.

#### 5. Conclusion and Future Directions

This study provides strong evidence that astronomical factors are not a static background influence but active, persistent, and quantifiable modulators of ENSO variability. The demonstrated bimodal, phase-dependent relationship between net shortwave radiation (RAD) and the Oceanic Niño Index (ONI) is consistent with secular changes in solar declination, establishing a robust physical mechanism linking orbital geometry to the ENSO energy budget.

These empirical findings indicate that integrating these significant astroclimatic parameters into current GCMs offers the missing physical constraint needed to resolve the SPB. This defines a new oscillatory framework for ENSO, in which external forcing—quantified via segmented RAD, governed by Short and Long Cycles—acts as a phase-specific predisposition, guiding the system toward ElNiño or LaNiña outcomes. Such a framework substantially enhances predictive skill for seasonal-to-decadal forecasting. Future research should focus on continuous, multi-centennial datasets to fully validate the long-term stability and persistence of this orbital—ENSO linkage.

#### **Data Availability**

Oceanic Niño Index (ONI) data for seasons were obtained from the NOAA Climate Prediction Center (2024), available at:

https://www.cpc.ncep.noaa.gov/products/analysis\_monitoring/ensostuff/ONI\_v5.php

Astronomical ephemerides, including Earth–Sun distance and solar declination, were calculated using the IMCCE Solar System ephemeris service via its Solar System Portal: (Orbital Ephemerides): <a href="https://ssp.imcce.fr/forms/ephemeris">https://ssp.imcce.fr/forms/ephemeris</a>

Dates of solstices and equinoxes were sourced from NASA's ModelE AR5 Simulations dataset provided by the Goddard Institute for Space Studies (GISS):

https://data.giss.nasa.gov/modelE/ar5plots/srvernal.html

Net downward shortwave radiation data were obtained from NASA's MERRA-2 reanalysis via the Goddard Earth Sciences Data and Information Services Center (GES DISC), using the open water net downward shortwave flux product for marine regions:

https://giovanni.gsfc.nasa.gov/giovanni

For further information on measurement definitions, see:

https://disc.gsfc.nasa.gov/information/glossary?title=Giovanni%20Measurement%20Definitions: %20Net%20Radiation

All datasets used in this study are openly accessible and were utilized in accordance with their respective data use policies. All graphics were generated by the author using publicly available datasets; no copyrighted or third-party material was reproduced.

#### References

- Cai, W.; McPhaden, M.J.; Grimm, A.M.; et al. Climate impacts of the El Niño–Southern Oscillation on South America. *Nat. Rev. Earth Environ.* 2020, 1, 215–231. doi:10.1038/s43017-020-0040-3.
- 2. Iizumi, T.; Luo, J.J.; Challinor, A.; et al. Impacts of El Niño Southern Oscillation on the global yields of major crops. *Nat. Commun.* **2014**, *5*, 3712. doi:10.1038/ncomms4712.
- 3. Xu, H.; Zhuang, C.C.; Oddo, V.M.; et al. Maternal preconceptional and prenatal exposure to El Niño Southern Oscillation levels and child mortality: a multi-country study. *Nat. Commun.* **2024**, *15*, 6034. doi:10.1038/s41467-024-50467-x.
- 4. Trenberth, K.E. The Definition of El Niño. Bull. Amer. Meteor. Soc. 1997, 78, 2771–2777.
- Lin, J.; Qian, T. A New Picture of the Global Impacts of El Nino-Southern Oscillation. *Sci. Rep.* 2019, 9, 17543. doi:10.1038/s41598-019-54090-5.
- 6. Le, T. Increased impact of the El Niño–Southern Oscillation on global vegetation under future warming. *Sci. Rep.* **2023**, *13*, 14459. doi:10.1038/s41598-023-41590-8.
- 7. Milanković, M. *Théorie Mathématique des Phénomènes Thermiques Produits par la Radiation Solaire*; Gauthier-Villars: Paris, France, 1920.
- 8. Agassiz, L. Discours sur les Glaciers; H. Riedo: Neuchâtel, Switzerland, 1837.
- 9. Lopes, F.; Courtillot, V.; Gibert, D.; Le Mouël, J.-L. Extending the Range of Milankovic Cycles and Resulting Global Temperature Variations to Shorter Periods (1–100 Year Range). *Geosciences* **2022**, 12, 448. doi:10.3390/geosciences12120448.
- 10. Smulsky, J. *Long-Term Changes in the Earth's Climate*; Cambridge Scholars Publishing: Newcastle upon Tyne, UK, **2021**.
- 11. NOAA Climate Prediction Center. Oceanic Niño Index (ONI) v5. **2024.** Available online: <a href="https://www.cpc.ncep.noaa.gov/products/analysis-monitoring/ensostuff/ONI-v5.php">https://www.cpc.ncep.noaa.gov/products/analysis-monitoring/ensostuff/ONI-v5.php</a>
- 12. Cordero, R.R.; Feron, S.; Damiani, A.; et al. Extreme fire weather in Chile driven by climate change and El Niño–Southern Oscillation (ENSO). *Sci. Rep.* **2024**, *14*, 1974. doi:10.1038/s41598-024-52481-x.
- 13. Mann, M.E.; Cane, M.A.; Zebiak, S.E.; Clement, A.C. Volcanic and Solar Forcing of the Tropical Pacific over the Past Millennium. *J. Clim.* **2005**, *18*, 447–456. doi:10.1175/JCLI-3276.1.
- 14. Wilcox, P.S.; et al. Solar Forcing of ENSO on Century Timescales. *Geophys. Res. Lett.* **2023**, *50*, e2023GL105201. doi:10.1029/2023GL105201.

- 15. Ljung, G.M.; Box, G.E.P. On a measure of lack of fit in time series models. *Biometrika* **1978**, *65*, 297–303. doi:10.1093/biomet/65.2.297.
- 16. Good, P. Permutation Tests: A Practical Guide to Resampling Methods for Testing Hypotheses, 2nd ed.; Springer: New York, NY, USA, 1994. doi:10.1007/978-3-319-02744-9.
- 17. Manly, B.F.J. *Randomization, Bootstrap and Monte Carlo Methods in Biology,* 3rd ed.; Chapman and Hall/CRC: Boca Raton, FL, USA, **2007**. doi:10.1201/9781315273075.
- 18. Romano, J.P.; Tirlea, M. Permutation testing for dependence in time series. *J. Time Ser. Anal.* **2022**, 43, 781–807. doi:10.1111/jtsa.12638.
- 19. Legendre, P.; ter Braak, C.J.F. Permutation tests for multifactorial analysis of variance. *Ecology* **2003**, *84*, 2517–2531.
- 20. Mann, M.E.; Lees, J.M. Robust estimation of background noise and signal detection in climatic time series. *Climatic Change* **1996**, *33*, 409–445. doi:10.1007/BF00142586.
- Cortés, J.; Saavedra, A.; Cressie, N. Accounting for Multiple Testing in the Analysis of Spatio-Temporal Environmental Data. *Environ. Ecol. Stat.* 2020, 27, 563–587. doi:10.1007/s10651-020-00446-4.
- 22. Mielke, P.W., Jr. Application of Multi-Response Permutation Procedures for Climate Pattern Analysis. *Mon. Weather Rev.* **1981**, *109*, 120–126.
- 23. Ptitsyn, A.A.; Zvonic, S.; Gimble, J.M. Permutation test for periodicity in short time series data. BMC Bioinformatics 2006, 7 (Suppl. 2), S10. doi:10.1186/1471-2105-7-S2-S10.
- French, J.P.; Székely, G.J.; Horváth, L. Spatiotemporal Functional Permutation Tests for Comparing Climate Behavior. *Adv. Stat. Climatol. Meteorol. Oceanogr.* 2024, 10, 123–137. doi:10.5194/ascmo-10-123-2024.
- Zhou, C.; Zwilling, C.E.; Calhoun, V.D.; Wang, M.Y. Efficient Blockwise Permutation Tests Preserving Exchangeability. *Int. J. Stat. Med. Res.* 2014, 3, 145–152. doi:10.6000/1929-6029.2014.03.02.8.
- 26. Winkler, A.M.; Ridgway, G.R.; Webster, M.A.; Smith, S.M.; Nichols, T.E. Permutation inference for the general linear model. *NeuroImage* **2015**, *92*, 381–397. doi:10.1016/j.neuroimage.2014.01.060.
- Lu, Z.; Schultze, A.; Carré, M.; et al. Increased frequency of multi-year El Niño–Southern Oscillation events across the Holocene. *Nat. Geosci.* 2025, 18, 337–343. doi:10.1038/s41561-025-01670-y.
- Huo, W.; Zhang, H.; Wu, T. Ascending phase of solar cycle 25 tilts the current El Niño–Southern oscillation transition. *Atmospheric and Oceanic Science Letters* 2024, 17, 100397. doi:10.1016/j.aosl.2023.100397.

- 29. Lopes, F.; Le Mouël, J.-L.; Courtillot, V.; Gibert, D. On the Shoulders of Laplace. *Phys. Earth Planet. Inter.* **2021**, *316*, 106693. doi:10.1016/j.pepi.2021.106693.
- 30. Lopes, F.; Courtillot, V.; Gibert, D.; Le Mouël, J.-L. On Two Formulations of Polar Motion and Identification of Its Sources. *Geosciences* **2022**, *12*, 398. doi:10.3390/geosciences12110398.
- 31. Lopes, F.; Courtillot, V.; Gibert, D.; Le Mouël, J.-L. On the Annual and Semi-Annual Components of Variations in Extent of Arctic and Antarctic Sea-Ice. *Geosciences* **2023**, *13*, 21. doi:10.3390/geosciences13010021.
- 32. Le Mouël, J.-L.; Lopes, F.; Courtillot, V. A Solar Signature in Many Climate Indices. *J. Geophys. Res. Atmos.* **2019**, *124*, 2600–2619. doi:10.1029/2018JD028939.
- 33. Le Mouël, J.-L.; Lopes, F.; Courtillot, V. A Strong Link between Variations in Sea-Ice Extent and Global Atmospheric Pressure? *The Cryosphere Discuss.* **2021**, *1*–28. doi:10.5194/tc-2021-216.
- 34. Courtillot, V.; Lopes, F.; Kossobokov, V.; Zuddas, P.; Gibert, D.; Boulé, J.-B.; Le Mouël, J.-L. On the Tilt of the Earth's Polar Axis (Climat): Some "Impressionist" Remarks. 2023, Preprint available online: arXiv:2310.02768.
- 35. Courtillot, V.; Lopes, F.; Gibert, D.; Boulé, J.-B.; Le Mouël, J.-L. On Variations of Global Mean Surface Temperature: When Laplace Meets Milanković. **2023**, Preprint available online: arXiv:2306.03442.

#### Acknowledgements

The author thanks Dr. Fernando Lopes for his insightful discussions and foundational contributions on solid Earth–atmosphere coupling, polar motion, and orbital influences on climate indices, which provided essential guidance for interpreting the astroclimatic mechanisms discussed in this study.

The author also acknowledges Sergio Salimbeni, Juan José Buela, Natalia V. Toscani Taberna (Universidad del Salvador), and Jorge R. Chinni for their valuable support throughout this work.

#### Author information

Authors and Affiliations

Facultad de Ingeniería, Universidad del Salvador, Pilar, Argentina

Guillermo A. Chinni

Ethics declarations. Competing interests

The authors declare no competing interests.

Funding: No external funding.

## **Figure Legends**

Figure 1 Observed vs. Estimated ONI series between 1999 and 2024.

Figure 2 Scatter plot of observed versus estimated ONI values for the 1999–2024 period.

**Figure 3** Residuals over time. The residuals fluctuate randomly around zero, showing no trend or autocorrelation, indicating that the SARIMA model effectively removed deterministic structure from the ONI series.

**Figure 4** Residuals histogram showing an approximately Gaussian, bell-shaped distribution, reinforcing the robustness of the SARIMAX framework.

**Figure 5** Decomposition of ONI variability (1999–2024) into the intrinsic component (SARIMA) and the external astroclimatic forcing (Exogenous component).

#### **Supplementary Information**

#### Materials and Methods

#### **Shortwave Radiation Dataset**

Net downward shortwave radiation over tropical Pacific waters was obtained from NASA's MERRA-2 reanalysis (product M2TMNXOCN v5.12.4) as monthly means with a spatial resolution of  $0.5^{\circ} \times 0.625^{\circ}$ , accessed via the Giovanni portal of the Goddard Earth Sciences Data and Information Services Center (GES DISC) (<a href="https://giovanni.gsfc.nasa.gov/giovanni">https://giovanni.gsfc.nasa.gov/giovanni</a>). Only marine grid cells were included, excluding land influence.

#### ENSO-phase-dependent contrast in the RAD field.

The chosen periods (2022–2024) represent the most recent, high-magnitude, and contrasting events (La Niña vs. El Niño) in the contemporary record, which optimally demonstrate the physical mechanism of differential shortwave flux (cloud-cover effect) that underpins the segmented  $X_{1,t}$  and  $X_{2,t}$  variables. The statistical significance of these variables, however, is derived from the full 26-year time series (1999–2024) employed in the SARIMAX model.

## Physical Justification of Bimodal Radiative Forcing

#### Full SARIMAX Model

or

$$ONI'_{t} = (\beta_{1}X_{1,t} + \beta_{2}X_{2,t}) + (\varphi_{1}ONI'_{t-1}) + (\Phi_{1}ONI'_{t-12} + \Phi_{2}ONI'_{t-24}) + (\theta_{1}w_{t-1} + \theta_{2}w_{t-2}) + w_{t}$$

$$ONI'_{t} = (\beta_{1} \cdot X_{1,t} + \beta_{2} \cdot X_{2,t}) + (\varphi_{1} \cdot ONI'_{t-1}) + (\Phi_{1} \cdot ONI'_{t-12} + \Phi_{2} \cdot ONI'_{t-24}) + (\theta_{1} \cdot w_{t-1} + \theta_{2} \cdot w_{t-2}) + w_{t-1}$$

#### **RAD Area Averaging and Segmentation**

The SARIMAX model employs two segmented exogenous variables,  $X_{1,t}$  (March–May) and  $X_{2,t}$  (June–February), derived from the open-water net downward shortwave radiation flux (RAD). This RAD flux is area-averaged over the equatorial Pacific region defined by 165° E–90° W and the latitude band 10° S to 5° N.

This specific latitudinal range (10° S to 5° N) was chosen because it optimally captures the ENSO-phase-dependent shifts in the mean radiation field. While standard ENSO indices often use 5° S to 5° N, extending the boundary to 10° S ensures inclusion of the maximum meridional extent of the La Niña cooling tongue and the full zonal cloud field response to ENSO forcing. This is critical for maximizing the signal of the bimodal radiative contrast proposed here. The two figures below illustrate the fundamental physical contrast that motivates the segmentation.

## **Contrasting RAD Distribution during ENSO Phases**

The following figures display the zonal-mean RAD distribution across the study band (10° S to 5° N) for contemporary El Niño and La Niña events, providing physical support for the two distinct RAD cycles. Relevance to Model: This contrast justifies the use of  $X_{2,t}$  to capture RAD variability during the phase where the system's internal damping mechanisms are dominant, leading to the observed negative correlation coefficient ( $\beta_2$ ).

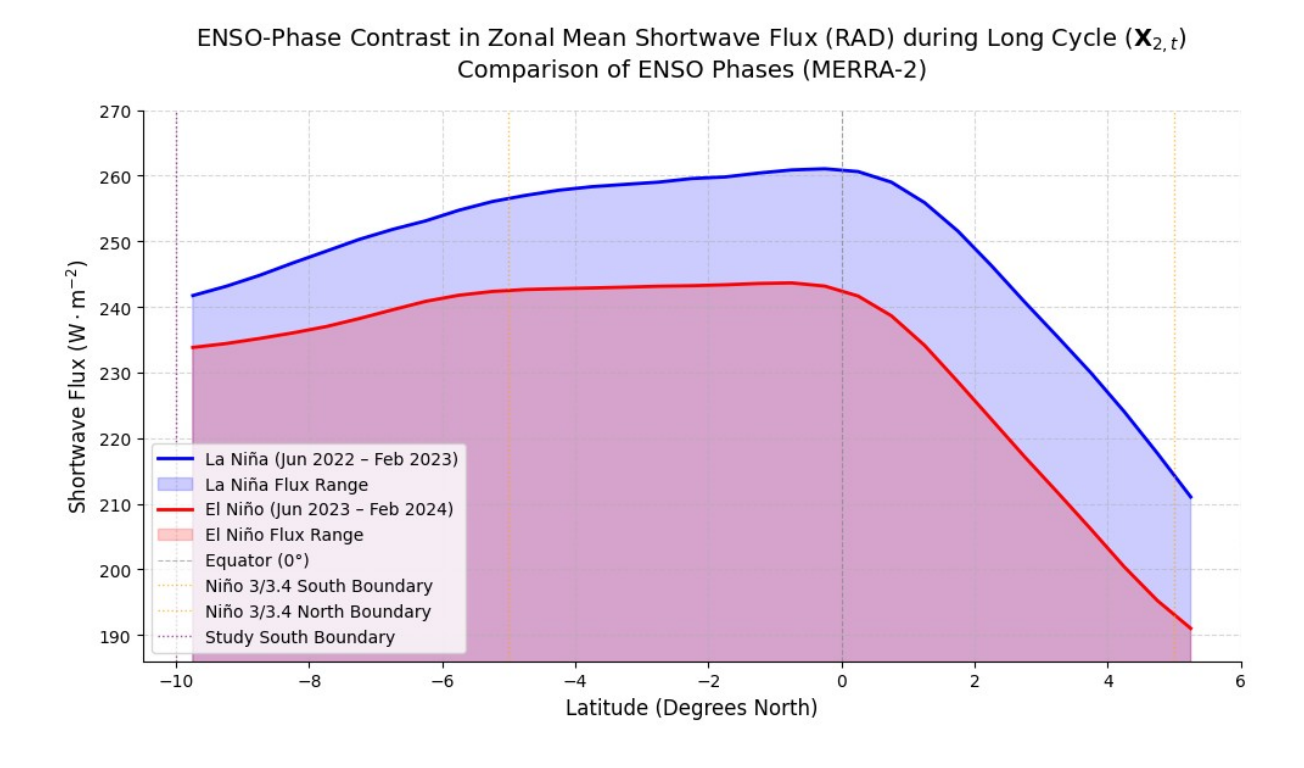


Figure S1. Long Cycle  $X_{2,t}$  (June–February) Contrast Observation: During the Long Cycle (the ENSO development phase), La Niña (blue) exhibits consistently and significantly higher RAD flux across the entire band compared to El Niño (red). This reflects the reduced cloudiness and atmospheric subsidence characteristic of the La Niña phase, allowing maximal shortwave transmission.

# ENSO-Phase Contrast in Zonal Mean Shortwave Flux (RAD) during Short Cycle ( $\mathbf{X}_{1,t}$ ) (Latitudinal Distribution: 165 ° E-90 ° W; MERRA-2 Reanalysis)

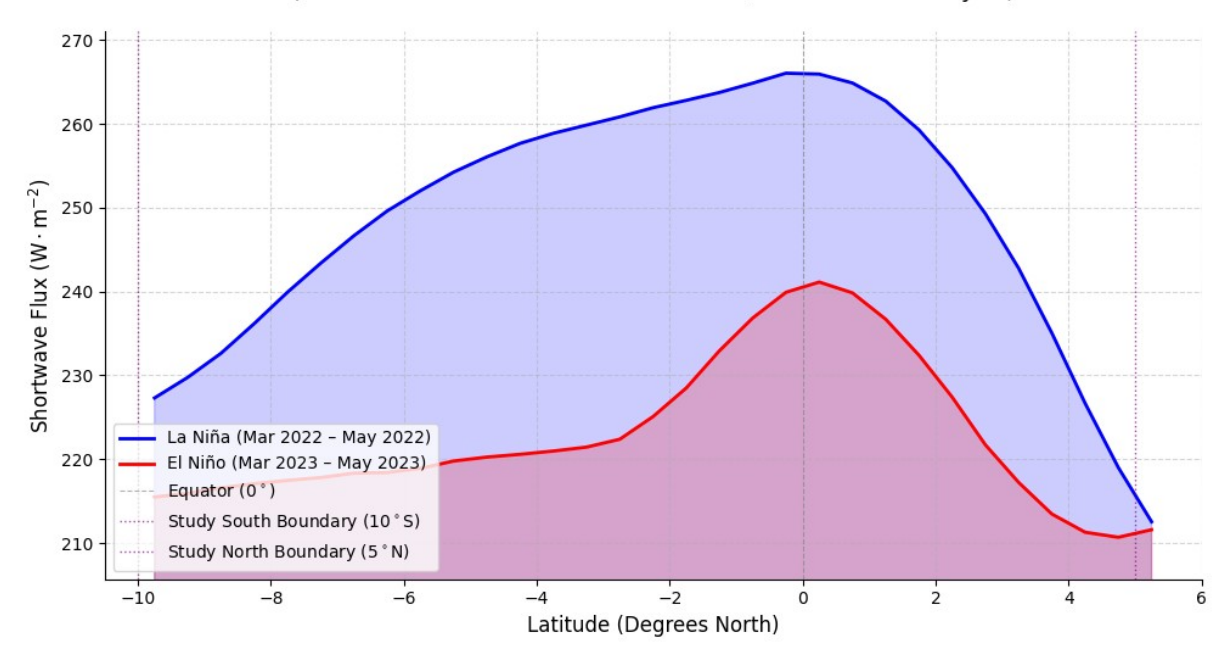


Figure S2. Short Cycle  $X_{1,t}$  (March–May) Contrast Observation: A similarly high contrast in RAD magnitude exists during the Short Cycle ((March–May)), the ENSO transition window. La Niña (blue) maintains a higher RAD flux due to suppressed convection, while El Niño (red) shows lower flux. The distribution demonstrates the system's sensitivity during this phase.

Relevance to Model: This substantial RAD contrast occurs precisely when oceanic thermal inertia is minimal (the predictability barrier). This visual evidence supports the hypothesis that a differential external energy input  $(X_{1,t})$  during this sensitive phase can act as an initial impulse, steering the ENSO system toward a warm or cold state, thus leading to the observed positive correlation coefficient  $(\beta_1)$ .

#### Summary table and permutation tests

hypothesis (P < 0.001).

Long\_cycle\_radiation

Note: The high standard P-values are characteristic of autoregressive time series: the non-parametric permutation test was used to provide a robust statistical inference, definitively rejecting the null

--- 1. SARIMAX BASE MODEL SUMMARY (For Official Report) ---Dep. Variable: Model: No. Observations: SARIMAX(1, 1, 2)x(2, 1, [], 12) Thu, 09 Oct 2025 17:34:45 Log Likelihood Date: AIC -327.751 03-01-1999 Sample: HQIC -315.921 - 12-01-2024 coef std err [0.025 0.975] Short\_cycle\_radiation 0.0014 0.001 -0.000 0.003 -1.514 7.706 4.658 0.001 0.130 -0.002 0.000 0.000 ma.L1 0.3767 0.081 0.535 0.218 ma.L2 0.3638 0.070 5.171 0.000 0.226 0.502 0.057 ar.S.L24 -0.3771 0.059 6.434 0.000 -0.492 -0.262 sigma2 0.0175 0.001 11.703 0.000 0.015 0.020 Ljung-Box (L1) (Q): 0.00 Jarque-Bera (JB): 3.09 Prob(Q): Heteroskedasticity (H): 0.96 Prob(JB): 0.21 Kurtosis: Prob(H) (two-sided): 0.89 2.92 --- STARTING/RESUMING PERMUTATION TESTS (N=1000) Permuting Short\_cycle\_radiation: 5%|| Permuting Short\_cycle\_radiation: 10%| 50/1000 [06:14<2:08:37, 8.12s/it][Checkpoint] Saved N=50 for Short cycle radiation. 100/1000 [12:34<2:15:58, 9.065/it][(heckpoint] Saved N=100 for Short\_cycle\_radiation. 150/1000 [19:04<2:06:31, 8.93s/it][(heckpoint] Saved N=150 for Short\_cycle\_radiation. Permuting Short\_cycle\_radiation: 15%| 20%| Permuting Short\_cycle\_radiation: Permuting Short\_cycle\_radiation: Permuting Short\_cycle\_radiation: 200/1000 [25:09<1:42:43. 7.70s/it][Checkpoint] Saved N=200 for Short cycle radiation. 25%| 30%| 250/1000 [23:03<1:42:43, 250/1000 [31:32<1:37:48, 300/1000 [37:47<1:33:32, 7.82s/it][Checkpoint] Saved N=250 for Short\_cycle\_radiation. 8.02s/it][Checkpoint] Saved N=300 for Short\_cycle\_radiation. 350/1000 [44:35<1:14:05, 400/1000 [50:55<1:06:20, 450/1000 [57:09<1:08:54, 6.84s/it][Checkpoint] Saved N=350 for Short\_cycle\_radiation. 6.63s/it][Checkpoint] Saved N=400 for Short\_cycle\_radiation. 7.52s/it][Checkpoint] Saved N=450 for Short\_cycle\_radiation. Permuting Short\_cycle\_radiation: Permuting Short\_cycle\_radiation: 35% Permuting Short cycle radiation: Permuting Short\_cycle\_radiation: Permuting Short\_cycle\_radiation: Permuting Short\_cycle\_radiation: 500/1000 [1:03:43<1:02:16, 7.47s/it][Checkpoint] Saved N=500 for Short\_cycle\_radiation.
550/1000 [1:10:18<58:45, 7.83s/it] [Checkpoint] Saved N=550 for Short\_cycle\_radiation.
600/1000 [1:16:51<58:38, 8.80s/it][Checkpoint] Saved N=600 for Short\_cycle\_radiation. 50% Permuting Short\_cycle\_radiation: Permuting Short\_cycle\_radiation: Permuting Short\_cycle\_radiation: 650/1000 [1:22:43<47:51, 700/1000 [1:29:17<42:32, 750/1000 [1:35:44<34:16, 8.20s/it][Checkpoint] Saved N=650 for Short\_cycle\_radiation. 8.51s/it][Checkpoint] Saved N=700 for Short\_cycle\_radiation. 8.23s/it][Checkpoint] Saved N=750 for Short\_cycle\_radiation. 8.42s/it][Checkpoint] Saved N=800 for Short\_cycle\_radiation. 8.18s/it][Checkpoint] Saved N=850 for Short\_cycle\_radiation. 6.41s/it][Checkpoint] Saved N=900 for Short\_cycle\_radiation. 6.46s/it][Checkpoint] Saved N=950 for Short\_cycle\_radiation. Permuting Short\_cycle\_radiation: Permuting Short\_cycle\_radiation: Permuting Short\_cycle\_radiation: 800/1000 [1:42:12<28:03, 850/1000 [1:48:26<20:26, 900/1000 [1:54:36<10:41, Permuting Short\_cycle\_radiation: 95%| Permuting Short\_cycle\_radiation: 100%| 950/1000 [2:00:41<05:22. 1000/1000 [2:07:10<00:00, 7.63s/it] [Checkpoint] Saved N=1000 for Short cycle radiation. Permuting Long\_cycle\_radiation: 50/1000 [04:49<1:29:47, 5.67s/it][Checkpoint] Saved N=50 for Long\_cycle\_radiation. 50/1000 [04:49x1:29:47, 5.67s/it][Checkpoint] Saved N=50 for Long\_cycle\_radiation. 100/1000 [10:47x1:40:41, 6.71s/it][Checkpoint] Saved N=100 for Long\_cycle\_radiation. 150/1000 [15:22x48:55, 3.45s/it][Checkpoint] Saved N=150 for Long\_cycle\_radiation. 200/1000 [20:05x68:37, 4.40s/it] [Checkpoint] Saved N=200 for Long\_cycle\_radiation. 250/1000 [24:30x1:13:28, 5.88s/it][Checkpoint] Saved N=200 for Long\_cycle\_radiation. 300/1000 [29:23x1:16:55, 6.59s/it][Checkpoint] Saved N=300 for Long\_cycle\_radiation. 350/1000 [34:30x1:09:07, 6.38s/it][Checkpoint] Saved N=350 for Long\_cycle\_radiation. 450/1000 [39:13x1:27:21, 8.77s/it][Checkpoint] Saved N=400 for Long\_cycle\_radiation. 500/1000 [44:22x56:46, 6.19s/it][Checkpoint] Saved N=450 for Long\_cycle\_radiation. 500/1000 [49:16x50:45, 6.09s/it][Checkpoint] Saved N=500 for Long\_cycle\_radiation. 550/1000 [5x1:7x1:04:01, 8.54s/it][Checkpoint] Saved N=500 for Long\_cycle\_radiation. Permuting Long\_cycle\_radiation:
Permuting Long\_cycle\_radiation:
Permuting Long\_cycle\_radiation: 10%| 15%| 20% Permuting Long\_cycle\_radiation:
Permuting Long\_cycle\_radiation:
Permuting Long\_cycle\_radiation: Permuting Long\_cycle\_radiation: Permuting Long\_cycle\_radiation: 40% Permuting Long\_cycle\_radiation: 500/1000 [49:16569:45, 6.095/it][Checkpoint] Saved N=500 for Long\_cycle\_radiation.
550/1000 [54:17<1:04:01, 8.545/it][Checkpoint] Saved N=550 for Long\_cycle\_radiation.
600/1000 [59:27<46:55, 7.045/it][Checkpoint] Saved N=600 for Long\_cycle\_radiation.
650/1000 [1:04:03:37:27, 6.425/it][Checkpoint] Saved N=600 for Long\_cycle\_radiation.
750/1000 [1:09:34<25:37, 5.135/it][Checkpoint] Saved N=700 for Long\_cycle\_radiation.
750/1000 [1:13:50<21:20, 5.125/it][Checkpoint] Saved N=750 for Long\_cycle\_radiation.
800/1000 [1:32:37<14:42, 5.885/it][Checkpoint] Saved N=800 for Long\_cycle\_radiation.
900/1000 [1:32:35<08:34, 5.155/it][Checkpoint] Saved N=800 for Long\_cycle\_radiation.
950/1000 [1:34:35<06:57, 8.365/it][Checkpoint] Saved N=900 for Long\_cycle\_radiation.
900/1000 [1:39:43<06:00, 5.385/it][Checkpoint] Saved N=950 for Long\_cycle\_radiation. Permuting Long\_cycle\_radiation:
Permuting Long\_cycle\_radiation:
Permuting Long\_cycle\_radiation: 55% Permuting Long\_cycle\_radiation: Permuting Long\_cycle\_radiation: 70% Permuting Long cycle radiation: Permuting Long\_cycle\_radiation: Permuting Long\_cycle\_radiation: 85% 90% 95% Permuting Long\_cycle\_radiation: 1000/1000 [1:39:43<00:00, 5.98s/it] 

*Figure S3.* Summary table and permutation tests processes and results.

## Oceanic Niño Index (ONI) Niño 3.4 region

Year	1.DJF	2.JFM	3.FMA	4.MAM	5.AMJ	6.MJJ	7.JJA	8.JAS	9.ASO	10.SON	11.OND	12.NDJ
1999	-1.5	-1.3	-1.1	-1.0	-1.0	-1.0	-1.1	-1.1	-1.2	-1.3	-1.5	-1.7
2000	-1.7	-1.4	-1.1	-0.8	-0.7	-0.6	-0.6	-0.5	-0.5	-0.6	-0.7	-0.7
2001	-0.7	-0.5	-0.4	-0.3	-0.3	-0.1	-0.1	-0.1	-0.2	-0.3	-0.3	-0.3
2002	-0.1	0.0	0.1	0.2	0.4	0.7	0.8	0.9	1.0	1.2	1.3	1.1
2003	0.9	0.6	0.4	0.0	-0.3	-0.2	0.1	0.2	0.3	0.3	0.4	0.4
2004	0.4	0.3	0.2	0.2	0.2	0.3	0.5	0.6	0.7	0.7	0.7	0.7
2005	0.6	0.6	0.4	0.4	0.3	0.1	-0.1	-0.1	-0.1	-0.3	-0.6	-0.8
2006	-0.9	-0.8	-0.6	-0.4	-0.1	0.0	0.1	0.3	0.5	0.8	0.9	0.9
2007	0.7	0.2	-0.1	-0.3	-0.4	-0.5	-0.6	-0.8	-1.1	-1.3	-1.5	-1.6
2008	-1.6	-1.5	-1.3	-1.0	-0.8	-0.6	-0.4	-0.2	-0.2	-0.4	-0.6	-0.7
2009	-0.8	-0.8	-0.6	-0.3	0.0	0.3	0.5	0.6	0.7	1.0	1.4	1.6
2010	1.5	1.2	0.8	0.4	-0.2	-0.7	-1.0	-1.3	-1.6	-1.6	-1.6	-1.6
2011	-1.4	-1.2	-0.9	-0.7	-0.6	-0.4	-0.5	-0.6	-0.8	-1.0	-1.1	-1.0
2012	-0.9	-0.7	-0.6	-0.5	-0.3	0.0	0.2	0.4	0.4	0.3	0.1	-0.2
2013	-0.4	-0.4	-0.3	-0.3	-0.4	-0.4	-0.4	-0.3	-0.3	-0.2	-0.2	-0.3
2014	-0.4	-0.5	-0.3	0.0	0.2	0.2	0.0	0.1	0.2	0.5	0.6	0.7
2015	0.5	0.5	0.5	0.7	0.9	1.2	1.5	1.9	2.2	2.4	2.6	2.6
2016	2.5	2.1	1.6	0.9	0.4	-0.1	-0.4	-0.5	-0.6	-0.7	-0.7	-0.6
2017	-0.3	-0.2	0.1	0.2	0.3	0.3	0.1	-0.1	-0.4	-0.7	-0.8	-1.0
2018	-0.9	-0.9	-0.7	-0.5	-0.2	0.0	0.1	0.2	0.5	0.8	0.9	0.8
2019	0.7	0.7	0.7	0.7	0.5	0.5	0.3	0.1	0.2	0.3	0.5	0.5
2020	0.5	0.5	0.4	0.2	-0.1	-0.3	-0.4	-0.6	-0.9	-1.2	-1.3	-1.2
2021	-1.0	-0.9	-0.8	-0.7	-0.5	-0.4	-0.4	-0.5	-0.7	-0.8	-1.0	-1.0
2022	-1.0	-0.9	-1.0	-1.1	-1.0	-0.9	-0.8	-0.9	-1.0	-1.0	-0.9	-0.8
2023	-0.7	-0.4	-0.1	0.2	0.5	0.8	1.1	1.3	1.6	1.8	1.9	2.0
2024	1.8	1.5	1.1	0.7	0.4	0.2	0.0	-0.1	-0.2	-0.3	-0.4	-0.5

Figure S4. Oceanic Niño Index (ONI) in the Niño 3.4 region, presented by season, month, and year, covering 1999–2024 (from DJF, January, to NDJ, December).

## Net Downward Shortwave Radiation flux (RAD) (W/m²)

Year	1.DJF	2.JFM	3.FMA	4.MAM	5.AMJ	6.MJJ	7.JJA	8.JAS	9.ASO	10.SON	11.OND	12.NDJ
1999	261	263	245	233	229	224	230	249	265	272	263	260
2000	269	270	246	225	218	221	229	243	262	268	268	253
2001	262	263	240	218	224	219	225	245	263	269	252	227
2002	248	248	243	224	228	214	227	234	243	248	236	222
2003	229	245	246	241	228	224	225	250	260	265	260	243
2004	240	259	228	219	232	213	222	242	253	256	254	238
2005	248	240	254	230	224	221	223	246	261	268	259	254
2006	253	253	248	223	228	215	226	241	252	255	248	238
2007	229	255	244	233	228	221	229	245	266	271	256	250
2008	250	266	249	232	230	216	224	244	256	266	252	255
2009	256	254	240	225	224	216	216	239	250	254	242	228
2010	227	217	227	221	228	223	230	246	263	270	265	254
2011	252	264	248	215	212	212	224	246	260	269	259	250
2012	255	256	230	207	214	210	214	240	252	258	249	242
2013	239	257	233	225	220	217	224	245	258	258	257	240
2014	246	256	240	217	219	207	224	241	259	262	257	237
2015	248	252	237	214	203	197	209	225	241	238	223	206
2016	211	215	214	211	221	217	227	249	265	274	265	252
2017	256	256	237	211	214	214	220	244	264	261	261	249
2018	263	249	254	248	235	221	222	245	256	262	247	235
2019	234	237	226	215	206	211	221	239	257	261	252	241
2020	231	235	240	224	229	223	227	243	263	266	260	248
2021	253	252	244	220	226	221	222	245	260	266	260	246
2022	248	266	262	248	238	222	227	246	262	269	259	247
2023	254	254	249	217	202	207	211	235	245	247	238	228
2024	242	236	234	221	225	215	222	241	256	262	264	247

*Figure S5.* Net downward shortwave radiation flux (RAD) in the Niño 3.4 region, 1999–2024, by month and season (DJF January to NDJ December). Values are rounded for processing.

#### **Solar Declination Data and Sources**

Supplementary Table: NASA Solar Declination at Equinoxes (2000–2024) [Degrees, Minutes, Seconds]

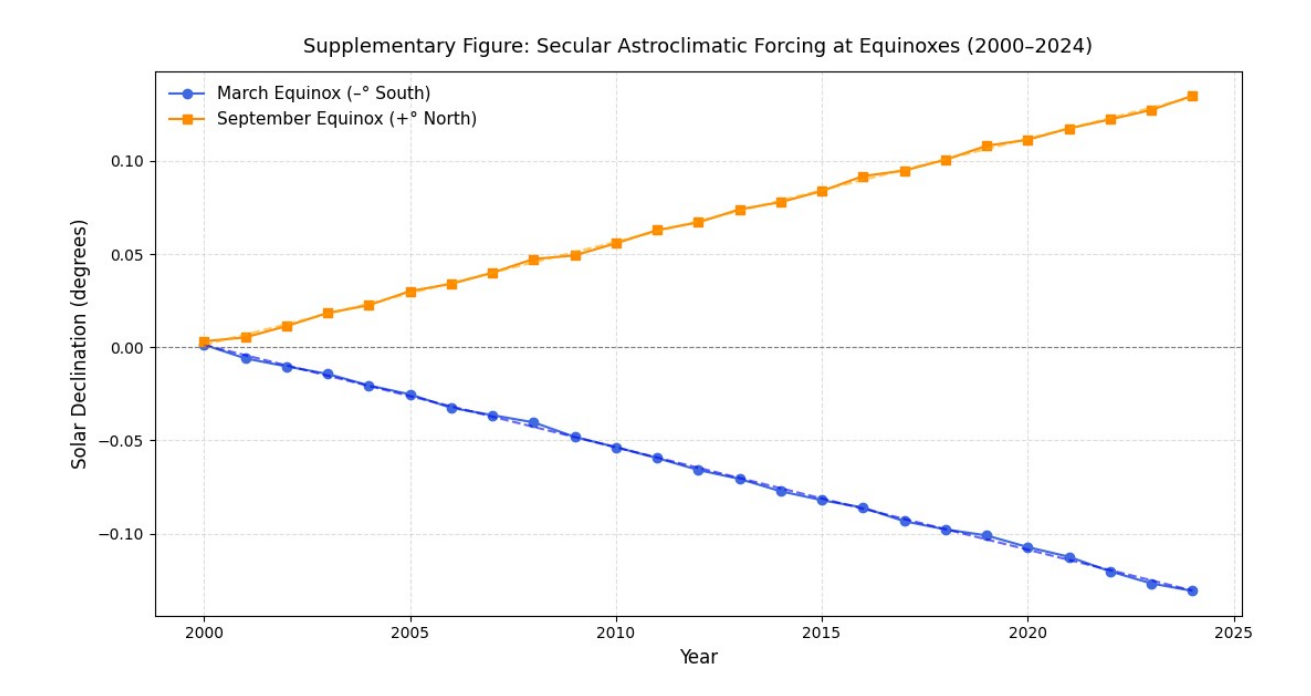
Year	Mar °	Mar'	Mar ''	Sep °	Sep '	Sep ''
2000	0	0	4.78	0	0	11.4
2001	-0	0	21.46	0	0	19.1
2002	-0	0	37.0	0	0	40.8
2003	-0	0	51.56	0	1	6.2
2004	-0	1	13.76	0	1	21.2
2005	-0	1	31.0	0	1	48.3
2006	-0	1	56.95	0	2	2.5
2007	-0	2	11.19	0	2	23.8
2008	-0	2	25.06	0	2	50.4
2009	-0	2	53.17	0	2	57.4
2010	-0	3	13.0	0	3	20.8
2011	-0	3	34.0	0	3	46.1
2012	-0	3	57.08	0	4	1.2
2013	-0	4	14.2	0	4	26.2
2014	-0	4	38.1	0	4	40.3
2015	-0	4	55.3	0	5	1.6
2016	-0	5	9.7	0	5	30.5
2017	-0	5	36.0	0	5	41.2
2018	-0	5	51.8	0	6	2.1
2019	-0	6	3.5	0	6	29.1
2020	-0	6	26.0	0	6	40.8
2021	-0	6	44.7	0	7	2.6
2022	-0	7	12.8	0	7	20.0
2023	-0	7	36.2	0	7	38.3
2024	-0	7	50.5	0	8	5.7

*Figure S6.* The table lists the solar declination at the March and September Equinoxes in degrees (°), minutes (′), and seconds (″), as well as the corresponding decimal degrees. This data highlights the progressive ±8 minutes of arc variation discussed in the main text.

Astronomical Ephemerides (Declination, Earth–Sun Distance): Calculated using the IMCCE Solar System ephemeris service via its Solar System Portal (Orbital Ephemerides).

Source URL: <a href="https://ssp.imcce.fr/forms/ephemeris">https://ssp.imcce.fr/forms/ephemeris</a>

Dates of Solstices and Equinoxes: Sourced from NASA's ModelE AR5 Simulations dataset provided by the Goddard Institute for Space Studies (GISS). Source URL: <a href="https://data.giss.nasa.gov/modelE/ar5plots/srvernal.html">https://data.giss.nasa.gov/modelE/ar5plots/srvernal.html</a>



Supplementary *Figure S7* visually represents the secular change in solar declination over 2000–2024 for both equinoxes, illustrating the gradual precession-driven movement of the Sun's apparent position along the ecliptic in each hemisphere.

## **Data Availability for Supplementary Information**

The datasets and ephemerides used in this supplementary analysis are the same as those described in the main manuscript's Data Availability section.